# Edge Solitons in a Nonlinear Mechanical Topological Insulator

David D. J. M. Snee[a], Yi-Ping Ma[a,*]

[a]*Department of Mathematics, Physics and Electrical Engineering, Northumbria University, Newcastle upon Tyne, NE1 8ST, UK.*

**Abstract**

We report localized and unidirectional nonlinear traveling edge waves in a 2D mechanical (phononic) topological insulator consisting of a collection of pendula with weak Duffing nonlinearity connected by linear springs. This is achieved by showing theoretically that the classical 1D nonlinear Schrödinger equation governs the envelope of 2D edge modes. The theoretical predictions from the 1D envelope equation are confirmed by numerical simulations of the original 2D system for various types of traveling waves and rogue waves. As a result of topological protection, these edge solitons persist over long time intervals and through irregular boundaries. The existence of topologically protected edge solitons may have significant implications on the design of acoustic devices.

*Keywords:* Phononics, Nonlinear structures, Topological protection, Acoustic wave phenomena
**Declarations of interest: none**

## 1. Introduction

The emerging field of topological mechanics utilizes topological principles to reveal new collective excitations in classical mechanical (phononic) systems [1, 2]. The definitive achievement in this field is the discovery of topological acoustic metamaterials, including in particular mechanical topological insulators (TIs). The theory of TIs was originally developed in condensed matter physics, with extensive literature on both one-dimensional and multi-dimensional systems [3, 4, 5]. The one stand out property of TIs which holds the ongoing interest in the topic is that a clear dichotomy exists between the edge (surface) and the bulk of the material as electrons are conducted only on the edge whilst the bulk is insulating. The existence of such edge states at the interface between two bulk materials with different topological invariants is guaranteed by the principle of bulk-edge correspondence [6, 7]. More recently, the theoretical framework underlying quantum TIs has been generalized to photonic systems governed by classical electromagnetic fields [8, 9, 10]. In analogy to electrons in traditional TIs, electromagnetic waves in photonic TIs propagate along the edge with very little backscattering, even in the presence of disorders such as missing site(s) on the edge of a photonic lattice [11, 12, 13].

The metamaterials in topological mechanics can be classified into two families depending on whether the topological edge modes appear at zero frequency or high frequencies [1]. In the zero frequency case, these edge modes are identified as floppy modes and self-stress states in Maxwell frames [14]. Here we focus on the high frequency case, where topologically protected transport via phonons is enabled. Seminal work in this direction includes analogues of the quantum Hall effect using a lattice of hanging gyroscopes [15], and the quantum spin Hall effect (QSHE) using a lattice of coupled pendula [16] and bi-layered lattices of disks and springs [17]. Topological phonons are subsequently classified based on local symmetries [18].

The existing literature on nonlinear topological mechanics notably includes establishment of topological solitons as the nonlinear mechanism for zero-frequency floppy modes to propagate through the bulk of a 1D Maxwell frame [19], and the effect of nonlinearity on the resonant characteristics of high-frequency edge modes in both 1D and 2D mechanical TIs [20]. However, the possibility of nonlinear waves remains open in the high-frequency case. The theory of nonlinear waves in continuous systems has already formed a cornerstone of nonlinear science [21]. A fundamental result is that in such systems, dispersion can balance with nonlinearity to produce robust localized nonlinear traveling waves known as solitons. The theory of nonlinear waves in discrete systems has flourished more recently, especially in

*Corresponding author.
*Email addresses:* david.snee@northumbria.ac.uk (David D. J. M. Snee), yiping.m@gmail.com (Yi-Ping Ma)

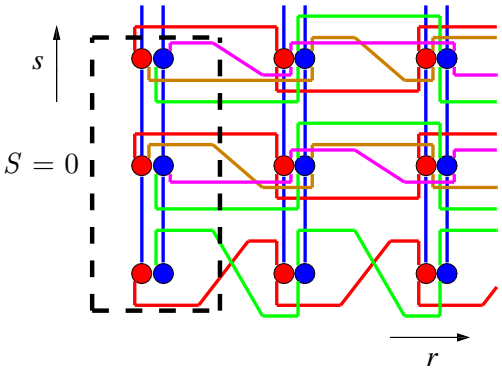


Figure 1: (Color online) Schematic view of the first unit cell $S = 0$ consisting of three sites on a generic lattice. The first, second, and third rows respectively represent $(x^{(0)}_{r,S}, y^{(0)}_{r,S})$, $(x^{(1)}_{r,S}, y^{(1)}_{r,S})$, and $(x^{(2)}_{r,S}, y^{(2)}_{r,S})$. Each site hosts an $x$ (red) and a $y$ (blue) pendulum carrying a mass. Simple springs in the $s$-direction connecting pendula are shown as blue lines. Couplings between pendula in the $r$-direction are shown as red and green lines. Cross couplings between the $x$ and $y$ pendula of neighboring sites are shown as brown and magenta lines. Negative couplings are realized via one lever arm, and positive couplings via two lever arms. Each pendulum $x^{(0)}_{r,S}$ or $y^{(0)}_{r,S}$ is connected to solid walls by springs. The edges are implemented by replacing the outside sites by solid walls. These walls are not shown for clarity.

the context of nonlinear optics and Bose-Einstein condensates [22]. In mechanical lattices, the study of nonlinear waves dates back to the classical 1D Fermi-Pasta-Ulam-Tsingou (FPUT) lattice [23], whose 1D and 2D extensions are still studied very recently [24, 25, 26]. Coupled pendula have been extensively studied in terms of synchronization and destabilization [27], while coherent structures therein such as breathers continue to capture considerable interest [28, 29, 30]. Nonlinear elastic metamaterials known as granular crystals have attracted much recent attention [31], with topological effects already demonstrated [32].

In this Letter, we use the theory of nonlinear waves to describe nonlinear interactions between high-frequency edge modes in a 2D mechanical TI. The primary aim is to discover topologically protected edge solitons (TPES), which are nonlinear traveling edge waves that inherit the topological protection of the corresponding linear system. Using dimension reduction and asymptotic analysis, the original 2D nonlinear system is reduced to the classical 1D nonlinear Schrödinger (NLS) equation [33]. This equation admits a plethora of soliton solutions, all of which correspond to TPES in the original system. Theoretical predictions are compared to numerical simulations on relatively large domains with excellent agreement. This practically enables robust transport of a mechanical state from one location to another on the edge of a generic 2D lattice. We remark that nonlinear topological edge states have already been reported in photonic Floquet TIs [34, 35, 36], polariton TIs [37, 38, 39], and classical optical networks [40], but our work represents a first step into the mechanical (phononic) world.

## 2. Mathematical Framework

The 2D mechanical TI we study is the one proposed by Süsstrunk and Huber [16], which is the first mechanical implementation of the QSHE. In the QSHE, two counter-propagating helical edge modes traverse the edge similarly with the exception of their spin degree of freedom [41, 42]. The QSHE model in [16] is two independent copies of the Hofstadter model [43] on the 2D square lattice indexed by $(r, s)$:

$$\hat{H} = \sum_{\alpha=\pm} \hat{H}_\alpha,$$
$$\hat{H}_\alpha = f_0 \sum_{r,s} \left( \hat{a}^\dagger_{r,s,\alpha} \hat{a}_{r,s+1,\alpha} + e^{i\alpha\Phi s} \hat{a}^\dagger_{r,s,\alpha} \hat{a}_{r+1,s,\alpha} + \text{H.c.} \right).$$

Here $\alpha$ is a spin index that labels the two copies, $f_0$ is the magnitude of the hopping amplitude, $\hat{a}^\dagger_{r,s,\alpha}$ and $\hat{a}_{r,s,\alpha}$ are respectively the creation and annihilation operators of a particle with spin $\alpha$ at site $(r, s)$, $\Phi = 2\pi/3$ is the magnetic flux, and H.c. denotes Hermitian conjugacy. This choice of $\Phi$ makes $\hat{H}$ periodic on a $1 \times 3$ unit cell, so the Hamiltonian matrix takes the form

$$H = \begin{pmatrix} H_+ & 0 \\ 0 & H_- \end{pmatrix},$$

where $H_\pm$ are $3 \times 3$ matrices. The key insight in [16] is that $H$ can be made positive-definite and real symmetric through a similarity transform to serve as the dynamical matrix for a system of coupled oscillators. This system is then realized on a 2D square lattice where each site contains two pendula $x_{r,s}$ and $y_{r,s}$ that are hinged to swing only in the $s$-direction, with linear springs attached to the pendula to achieve couplings in both $s$- and $r$-directions. In the following, we group the sites in the $s$-direction into unit cells indexed by $S$, with each cell consisting of three sites $(x^{(j)}_{r,S}, y^{(j)}_{r,S})$, $j = 0, 1, 2$.

In [16], linear equations of motion are presented for this system; here we include an additional cubic (Duffing) nonlinearity inherent to pendula, which yields

$$\ddot{x}^{(0)}_{r,S} = -(\omega_0^2 + Af)x^{(0)}_{r,S} + \sigma(x^{(0)}_{r,S})^3 + f(x^{(0)}_{r+1,S} + x^{(0)}_{r-1,S} + x^{(1)}_{r,S} + x^{(2)}_{r,S-1}), \quad (1)$$

$$\ddot{y}^{(0)}_{r,S} = -(\omega_0^2 + Af)y^{(0)}_{r,S} + \sigma(y^{(0)}_{r,S})^3 + f(y^{(0)}_{r+1,S} + y^{(0)}_{r-1,S} + y^{(1)}_{r,S} + y^{(2)}_{r,S-1}), \quad (2)$$

$$\ddot{x}^{(1)}_{r,S} = -(\omega_0^2 + Af)x^{(1)}_{r,S} + \sigma(x^{(1)}_{r,S})^3 + f(x^{(0)}_{r,S} + x^{(2)}_{r,S}) - \frac{f}{2}(x^{(1)}_{r+1,S} + x^{(1)}_{r-1,S}) + \frac{\sqrt{3}f}{2}(y^{(1)}_{r+1,S} - y^{(1)}_{r-1,S}), \quad (3)$$

$$\ddot{y}^{(1)}_{r,S} = -(\omega_0^2 + Af)y^{(1)}_{r,S} + \sigma(y^{(1)}_{r,S})^3 + f(y^{(0)}_{r,S} + y^{(2)}_{r,S}) - \frac{f}{2}(y^{(1)}_{r+1,S} + y^{(1)}_{r-1,S}) + \frac{\sqrt{3}f}{2}(-x^{(1)}_{r+1,S} + x^{(1)}_{r-1,S}), \quad (4)$$

$$\ddot{x}^{(2)}_{r,S} = -(\omega_0^2 + Af)x^{(2)}_{r,S} + \sigma(x^{(2)}_{r,S})^3 + f(x^{(0)}_{r,S+1} + x^{(1)}_{r,S}) - \frac{f}{2}(x^{(2)}_{r+1,S} + x^{(2)}_{r-1,S}) + \frac{\sqrt{3}f}{2}(-y^{(2)}_{r+1,S} + y^{(2)}_{r-1,S}), \quad (5)$$

$$\ddot{y}^{(2)}_{r,S} = -(\omega_0^2 + Af)y^{(2)}_{r,S} + \sigma(y^{(2)}_{r,S})^3 + f(y^{(0)}_{r,S+1} + y^{(1)}_{r,S}) - \frac{f}{2}(y^{(2)}_{r+1,S} + y^{(2)}_{r-1,S}) + \frac{\sqrt{3}f}{2}(x^{(2)}_{r+1,S} - x^{(2)}_{r-1,S}). \quad (6)$$

Here $A = 3 + \sqrt{3}$, $f$ describes the linear restoring forces of the springs, and $\omega_0$ and $\sigma$ respectively describe the linear and nonlinear parts of the restoring forces of pendula. Consistent with [16] we choose $\omega_0 = 3\pi/2$ and $f = 4.16\pi^2$. The nonlinear coefficient $\sigma$ is found by expanding the restoring force of the pendulum, i.e. $-\omega_0^2 \sin(\theta) \approx -\omega_0^2\theta + \frac{\omega_0^2}{6}\theta^3$, which gives $\sigma = \frac{\omega_0^2}{6}$.

Figure 1 shows a schematic view of the couplings on a generic lattice with the first unit cell ($S = 0$) emphasized. Hereafter we consider the compact matrix form

$$\ddot{\boldsymbol{X}}_{r,S}(t) = (\boldsymbol{\mathcal{L}}\boldsymbol{X})_{r,S} + \sigma\boldsymbol{\mathcal{N}}_{r,S} \quad (7)$$

where $\boldsymbol{X} = [x^{(0)}, y^{(0)}, x^{(1)}, y^{(1)}, x^{(2)}, y^{(2)}]^T$, $t$ denotes time, $\cdot$ denotes time derivative, $\boldsymbol{\mathcal{L}}$ is the linear operator encoding the couplings of the system, $\sigma$ is the strength of the Duffing nonlinearity, and $\boldsymbol{\mathcal{N}} = \boldsymbol{X}^3$. Unless otherwise specified, the 2D domain is taken to be rectangular with $N_r$ sites in the $r$-direction, $r = 0, 1, 2, \cdots, N_r - 1$, and $N_S$ unit cells in the $S$-direction, $S = 0, 1, 2, \cdots, N_S - 1$. On a 1D domain with $\boldsymbol{\mathcal{L}}$ chosen as the discrete Laplacian, Eq. (7) reduces to the 1D nonlinear Klein-Gordon equation with a cubic nonlinearity [44], from which the 1D NLS equation can be derived using the method of multiple scales [21]. Here we combine this procedure with dimension reduction to derive a 1D amplitude equation from the general 2D system given by Eq. (7).

In the linear problem ($\sigma = 0$), to describe an edge state of a specific boundary, say along $S$, we take the Fourier transform $\boldsymbol{X}_{r,S}(t) = e^{i\theta}\boldsymbol{X}^E_r + c.c$, $c.c$ denoting complex conjugacy, where the exponent $\theta = Sk - t\alpha(k)$, with $k$ being the wavenumber in $S$ (along the edge), $\alpha(k)$ being the dispersion relation, and $\boldsymbol{X}^E_r$ being the 1D edge state that decays in $r$ (perpendicular to the edge). This reduces Eq. (7) to the eigenvalue problem

$$\boldsymbol{\mathcal{L}}(k)\boldsymbol{X}^E_r = -\alpha(k)^2\boldsymbol{X}^E_r, \quad (8)$$

where $\boldsymbol{\mathcal{L}}(k)$ denotes the 1D linear operator after the Fourier transform, and $\boldsymbol{X}^E_r$ is normalized such that $\|\boldsymbol{X}^E_r\|_2^2 = \sum_j |\boldsymbol{X}^E_j|^2 = 1$. In the nonlinear problem ($\sigma \neq 0$), similarly to [34, 35], we aim to construct a weakly nonlinear edge mode. Since Eq. (7) does not have a small parameter, we must introduce the small parameter in the initial condition. This is achieved by considering the spectral envelope with a narrow width $0 < \epsilon \ll 1$ at carrier wavenumber $k = k_0$ and carrier frequency $\alpha_0 \equiv \alpha(k_0)$, in the reference frame co-moving with the group velocity of the envelope $\alpha'_0 \equiv \alpha'(k_0)$. Specifically, we choose a multiple scale ansatz for the weakly nonlinear edge mode of the form

$$\boldsymbol{X}(r, S, \tilde{S}, t, \tau) = \epsilon\left\{C(\tilde{S}, \tau)e^{i(Sk_0 - t\alpha_0)}\boldsymbol{X}^E_r + c.c\right\} + O(\epsilon^2), \quad (9)$$

where $C(\tilde{S}, \tau)$ is the scalar envelope function and evolves in the slow variables $\tilde{S} \equiv \epsilon(S - \alpha'_0 t)$ and $\tau \equiv \epsilon^2 t$. Thus, the time and space differential operators are now written as $\partial_t = \epsilon^2\partial_\tau - \epsilon\alpha'_0\partial_{\tilde{S}} - \alpha_0 i$ and $\partial_S = \epsilon\partial_{\tilde{S}} + k_0 i$ respectively.

The dispersion relation $\alpha(k)$, $k \in [0, 2\pi)$, numerically computed by solving Eq. (8) on a finite 1D domain, is shown in Fig. 2. The bulk (continuous) spectrum consists of three bands (blue), and the edge (point) spectrum exist in the two gaps (red). Thus, for each wavenumber $k$ there are precisely six point eigenvalues, three in either gap, whose corresponding eigenfunctions are the edge states that decay in $r$. The topologically protected edge states are those in the bulk band gap, or more precisely the range of $\alpha$ where the only permissible states are the pair of counterpropagating helical edge states.

One can now substitute the ansatz (9) directly into Eq. (7) and expand asymptotically in $\epsilon$. In particular, we

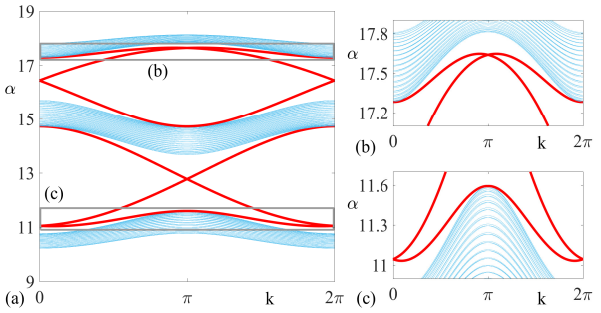


Figure 2: (Color online) The dispersion relation $\alpha(k)$ computed on the left/right edge of a rectangular lattice with $N_r = 60$ sites in the $r$-direction. The bulk spectrum is shown in blue and the edge spectrum is shown in red. In the latter, each eigenvalue corresponds to a pair of edge states localized respectively on the left and on the right.

expand the dispersion relation $\alpha(k)$ around the carrier wavenumber $k_0$ in operators form as

$$\alpha(k) = \alpha_0 - i\alpha_0'\epsilon\partial_{\tilde{S}} - \frac{1}{2}\alpha_0''\epsilon^2\partial_{\tilde{S}\tilde{S}} + O(\epsilon^3), \tag{10}$$

where $\alpha_0'' \equiv \alpha''(k_0)$. At $O(\epsilon)$ and $O(\epsilon^2)$ the equations are trivial. To leading nontrivial order, at $O(\epsilon^3)$, taking the inner product of both sides of the equation with $\boldsymbol{X}_r^E$, where the inner product is defined as $\langle \boldsymbol{g}, \boldsymbol{h}\rangle = \sum_j g_j^* h_j$, then the 1D classical second-order NLS equation appears in canonical form:

$$iC_\tau + \frac{\alpha_0''}{2}C_{\tilde{S}\tilde{S}} + \frac{3\tilde{\sigma}}{2\alpha_0}|C|^2 C = 0, \tag{11}$$

where $\tilde{\sigma} = \sigma\|\boldsymbol{X}_r^E\|_4^4 \equiv \sigma\sum_j |\boldsymbol{X}_j^E|^4$. The NLS equation is a maximally balanced equation and is focusing or defocusing if $\alpha_0''\alpha_0/\tilde{\sigma} > 0$ or $\alpha_0''\alpha_0/\tilde{\sigma} < 0$ respectively.

## 3. Numerical Simulations

The propagation of different types of edge solitons around the boundaries of the mechanical lattice can now be investigated by numerically solving Eq. (7) with the following initial condition resulting from the ansatz (9)

$$\boldsymbol{X}_{r,S}(t=0) = \epsilon C(S)e^{iSk_0}\boldsymbol{X}_r^E + c.c, \tag{12}$$

where $C(S)$ represents the initial envelope needed to produce the desired soliton solution to Eq. (11). Note that the envelope $C(S)$ quantifies the inter-cell variation of the pulse shape along the edge, whilst the eigenstate $\boldsymbol{X}_r^E$ quantifies both the decay of the pulse shape into the bulk and the intra-cell variation between the three sites forming the unit cell. Hereafter we take $\epsilon = 0.1$ and explore different choices of the carrier wave as specified by $(k_0, \alpha_0)$ with different types of envelopes $C(S)$.

### 3.1. Traveling Edge Solitons

First, we consider the focusing case where Eq. (11) admits a two-parameter family of bright solitons [33], where the two parameters can be taken as $k_0$ and $\epsilon$. The bright soliton is a classical solution of the 1D NLS equation that can be obtained directly from the inverse scattering transform [45]. The focusing condition implies that bright solitons exist only for a finite interval of $k_0$; at each value of $k_0$, fixing the spectral width $\epsilon$ fixes the amplitude of the wave packet. The 2D bright edge soliton can be obtained by considering the initial condition (12) with the scalar envelope function

$$C_B(S) = \Lambda\,\mathrm{sech}\left(\epsilon(S - S_0)\right), \tag{13}$$

where $\Lambda = \sqrt{2\alpha_0\alpha_0''/3\tilde{\sigma}}$ and $S_0$ represents the initial location of the wave packet. According to the theory, since the evolution is asymptotically governed by the 1D NLS equation, the bright edge soliton should persist at least until $t \sim O(\epsilon^{-2})$. In particular, the edge soliton should maintain its shape better at the theoretically predicted amplitude in comparison to smaller or greater amplitudes, which we show in Fig. S1(b) and Fig. S1(c) in Supplementary Material [46]. We remark that linear edge modes correspond to the limit $\Lambda \to 0$, which exhibits even more dispersion than Fig. S1(b). At a large time scale, the asymptotic theory may produce errors that eventually destroy the soliton profile.

To portray these edge solitons we introduce an excitation variable $z_{r,S}^{(i)} = \sqrt{(x_{r,S}^{(i)})^2 + (y_{r,S}^{(i)})^2}$, for $i = 0, 1, 2$, that represents the intensity of each site in the lattice. The propagation of a bright edge soliton at $(k_0, \alpha_0) = (2.827, 12.506)$ is shown in Fig. 3(a) where we express the intensity on the four edges of the rectangular lattice; the nonlinear wave traverses the boundaries of the mechanical lattice clockwise with almost no energy loss at the corners. This showcases both the topological protection of the traveling wave and the robustness of the soliton profile.

Akin to bright solitons in focusing NLS, there exists dark soliton solutions to defocusing NLS [33], i.e. the $\alpha_0''\alpha_0/\tilde{\sigma} < 0$ case in Eq. (11). Whereas a bright soliton is a localized rise of energy on a zero background, a dark soliton is a localized dip in energy on a non-zero background. The initial condition for a dark edge soliton is then given as Eq. (12) with the envelope function

$$C_D(S) = \Lambda\tanh(\epsilon(S - S_0)). \tag{14}$$

Such a dark edge soliton described by NLS also exists in for example polariton TIs [38, 39], but its propagation around a non-periodic 2D domain has not been explicitly demonstrated due to the difficulty to initialize the

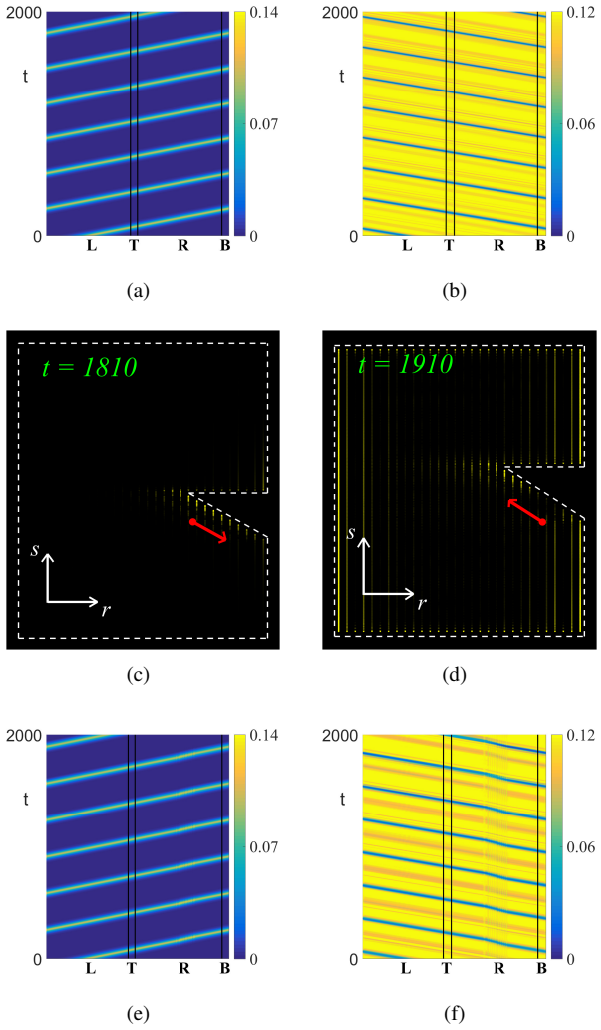


Figure 3: (Color online) Propagation of bright and dark edge solitons. The 2D domain consists of $N_r$ sites in the $r$-direction and $N_S$ unit cells in the $S$-direction. (a,c,e) A bright edge soliton on a rectangular lattice of size $N_r \times N_S = 30 \times 120$. The carrier wavenumber and frequency are $(k_0, \alpha_0) = (2.827, 12.506)$, which leads to soliton amplitude $\Lambda = 1.376$ in Eq. (13). (b,d,f) A dark edge soliton on a rectangular lattice of size $N_r \times N_S = 30 \times 101$. The carrier wavenumber and frequency are $(k_0, \alpha_0) = (2.146, 13.616)$, which leads to soliton amplitude $\Lambda = 1.705i$ in Eq. (14). Panels (a,b) show space-time plots along the edges of a full rectangular domain, where $L$, $T$, $R$ and $B$ correspond respectively to left, top, right, and bottom edges of the 2D lattice. Panels (c,d) show snapshots of a respective bright (c) and dark (d) edge soliton on a rectangular domain with a sharp turn cut out of the right edge; red arrows indicate the centre of the soliton envelope and its direction of travel. Panels (e,f) show space-time plots along the edges of the irregular domain in panels (c,d). Video simulations of (a-f) can be seen in Supplementary Material [46].

non-zero background. Here, we realize in Fig. 3(b) a dark edge soliton at $(k_0, \alpha_0) = (2.146, 13.616)$ traveling on a rectangular domain with little energy loss over a long time interval. See Supplementary Material [46] for another type of traveling wave known as the gray soliton [33]. Next we outline the rationale behind the construction of the initial condition, which also reveals the origin of the topological protection of edge solitons.

### *3.2. Topological Protection*

Assume that a finite 2D domain is dominated by a particular type of edge, e.g. the left and right edges in Fig. 3(a–b). Near a topologically protected frequency, the eigenfrequencies and the corresponding eigenfunctions on this 2D domain should match up well with those on a semi-infinite 2D periodic stripe with this type of edge. In the presence of weak nonlinearity, the envelope equation for the edge solitons on such a finite 2D domain should then be well approximated by the NLS equation on the corresponding 1D periodic domain. Thus, a unidirectionally traveling 1D NLS soliton corresponds to a unidirectionally looping 2D edge soliton insensitive to the details of the 2D domain. The detailed method to construct the edge soliton is described in Supplementary Material [46].

Let us now consider irregular domains, for instance by carving a sharp turn into the right edge of the lattice (the edge opposite the initial condition) and evolving the system using the same edge soliton initial conditions as in Fig. 3(a,b). Since the carrier wave is topologically protected, we expect that the nonlinear structures will traverse the domain with little to no backscattering regardless of the boundary type. This is seen in Fig. 3(c,d) where snapshots of the 2D domain show the edge solitons traverse the irregular domain in their last cycle before $t = 2000$. The space-time plots in Fig. 3(e,f) also show the edge solitons passing through the sharp turn of the right edge multiple times with little change in the pulse shape. The same is found to occur for rough boundaries with finer length scales, such as a Cantor-like function carved into the same edge, as shown in Supplementary Material [46]. These numerical experiments all but confirm the general principle that weakly nonlinear edge solitons inherit the topological protection of linear edge modes.

To further show the topological protection of edge solitons around different types of corners, we perform a numerical scattering analysis on bright solitons propagating on the above two types of domains over a long time period, say $t \in [0, 1 \times 10^4]$. Since the two parameters characterizing the bright solitons are $k_0$ and $\epsilon$, we consider varying them away from those in Fig. 3(a,c,e), i.e. $k_0 = 2.827$ and $\epsilon = 0.1$.

Firstly, we fix $k_0 = 2.827$ and compare the three cases $\epsilon = 0.05$, $\epsilon = 0.1$, and $\epsilon = 0.2$. Figure 4(a,b) respectively show the relative energy (the $L^2$-norm of $z$ on the left edge relative to its initial value) and the maximum amplitude (the $L^\infty$-norm of $z$ on the left edge) over 25 propagation cycles on the rectangular domain (R) and the domain with a wedge carved into the right edge (W). The most remarkable feature is that neither the energy nor the amplitude changes significantly, regardless of the domain shape. Thus, although these edge solitons are formally derived on the $O(\epsilon^{-2})$ time scale, they persist much longer in practice. It can also be seen that a larger $\epsilon$ causes the amplitude to oscillate more, while a smaller $\epsilon$ causes the energy to decay more. To explain these, we recall that $\epsilon$ is the spectral width and $\epsilon^{-1}$ is the physical width of the soliton. A larger $\epsilon$ causes greater interference between the two spectral envelopes centered at $k_0$ and $2\pi - k_0$ that form the soliton. This is a unique property of mechanical systems as opposed to optical systems, which will be further explored elsewhere. On the other hand, a smaller $\epsilon$ makes the soliton more spatially extended and thus causes the energy to spread more onto the other edges.

Next, we fix $\epsilon = 0.1$ and vary $k_0$ with the stipulation that it belongs to the topologically protected and focusing regime. In this band gap, the topologically protected set of wavenumbers is $k \in [1.573, 4.178]$ and the focusing set of wavenumbers is $k \in [0, 3.483]$. As such, in Fig. 4(c,d) we compare the three cases $k_0 = 2.199$, $k_0 = 2.513$, and $k_0 = 2.827$ on the two types of domains. The soliton can be seen to propagate very well as long as its carrier wavenumber lies in the interior of the allowable set of wavenumbers. The wavenumbers closer to the bulk appear to be more sensitive to the irregularity of the domain shape, as seen in Fig. 4(d).

Remarkably, linear edge modes disperse differently depending on the deformity shape, but nonlinear edge solitons maintain their profiles independent of the deformity shape. The system thus functions as a nonlinear acoustic cloak; see [47] for a similar proposal of a nonlinear optical cloak. In experiments, any waveform such as Eqs. (13–14) can be generated at a single site and propagated around the finite domain [16]. The required experimental setup is no different from that in the original experiment [16], only on a suitably larger domain to accommodate the narrow spectral envelope.

### *3.3. Rogue Edge Solitons*

Finally, we explore rational solutions to the classical 1D NLS equation, commonly known as rogue waves as they have recently proven to be very promising contenders for modeling waves with abnormally large

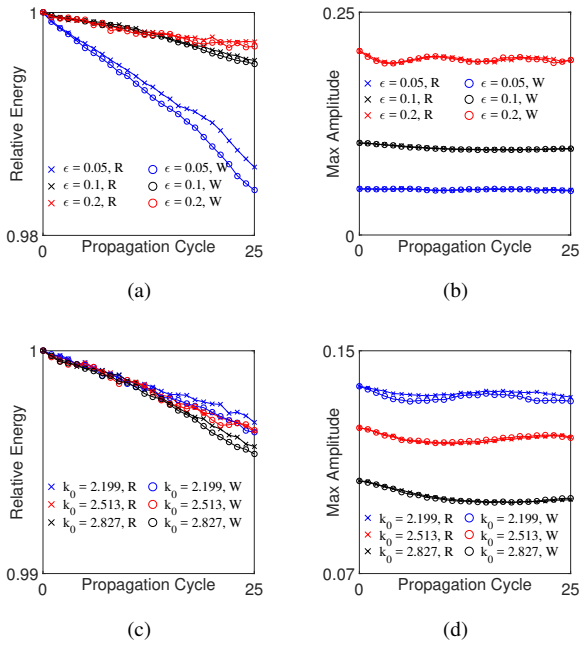


Figure 4: (Color online) Numerical scattering analysis for bright solitons. Panels (a,b) show the effect of fixing $k_0 = 2.827$ and varying $\epsilon = 0.05$ (blue), $\epsilon = 0.1$ (black), $\epsilon = 0.2$ (red) over multiple propagation cycles on two different domains. Domain $R$ is the fully rectangular domain, whilst domain $W$ is the domain with a wedge carved into the right edge. (a) Total energy of the solitons at each cycle relative to the initial value. (b) The maximum amplitude of the solitons at each cycle. Similarly, panels (c,d) show the effect of fixing $\epsilon = 0.1$ and varying $k_0 = 2.199$ (blue), $k_0 = 2.513$ (red), $k_0 = 2.827$ (black) on the two different domains.

heights [48, 49, 50, 51]. We first consider the famous Peregrine soliton [52] which is the prototypical example of a rogue wave solution. For visualization purposes, we require the maximum amplitude to appear at some $t > 0$, say $t_0 = 1200$. Therefore we shift the temporal variable by $t_0$ and consider the initial condition (12) with the envelope function given by

$$C_P(S) = \Lambda\left[1 - \frac{4(1 - 2i\tilde{t}_0)}{1 + 4\epsilon^2(S - S_0)^2 + 4\tilde{t}_0^2}\right]e^{i\tilde{\theta}}, \qquad (15)$$

where $\tilde{\theta} = \alpha_0 t_0 - \tilde{t}_0$ and $\tilde{t}_0 = \epsilon^2 \alpha_0'' t_0$. Figure 5(a) shows the appearance of the Peregrine edge soliton with the carrier wavenumber and frequency $(k_0, \alpha_0) = (2.334, 12.113)$. We note that the peak does indeed appear at $t \approx t_0$ according to the numerics.

Let us also consider the Kuznetsov-Ma (K-M) soliton, which was first derived by Ma [53] as a breathing wavepacket in time embedded in a plane wave solution. To generate a K-M edge soliton, we replace the envelope function in the initial condition (12) by the K-M

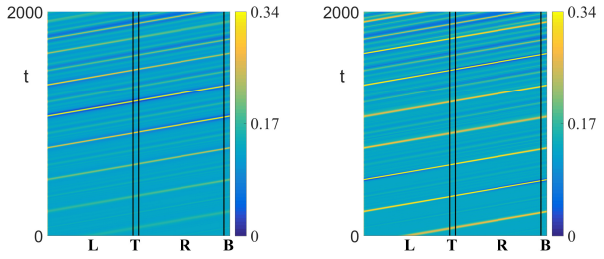


Figure 5: (Color online) Propagation of rogue edge solitons. Panel (a) shows a space-time plot of a Peregrine soliton described by Eq. (15) that peaks at $t \approx 1200$. Panel (b) shows a Kuznetsov-Ma edge soliton described by Eq. (16), peaking at $t_0 = 500$ with modulation parameter $\phi = 1$, with a breathing period of about 1000. The carrier wavenumber and frequency of both rogue waves are $(k_0, \alpha_0) = (2.334, 12.113)$, and the size of the rectangular domain is $N_r \times N_S = 20 \times 100$.

expression seen in [50], i.e.

$$C_{KM}(S;\phi) = \Lambda\left[\frac{\cos(\Omega\tilde{t}_0 + 2i\phi) - \cosh\phi\cosh\bar{S}}{\cos(\Omega\tilde{t}_0) - \cosh\phi\cosh\bar{S}}\right]e^{i\tilde{\theta}}, \tag{16}$$

where $\bar{S} = P\epsilon(S - S_0)$, $P = 2\sinh\phi$, $\Omega = \sinh 2\phi$, and $\phi$ is the real modulation parameter defining the breathing period. Figure 5(b) shows the appearance of a K-M edge soliton with $\phi = 1$ and $(k_0, \alpha_0) = (2.334, 12.113)$. We see that the breathing period agrees with the theory.

Note that since the carrier wave belongs to the topologically nontrivial regime, the propagation of these rogue edge solitons in the mechanical lattice is topologically protected, just like the traveling edge solitons presented earlier. See Supplementary Material [46] for another type of rogue wave known as the Akhmediev breather [54]. See also [55] for rogue waves in the FPUT lattice and granular crystals through reduction to NLS.

## 4. Discussion and Summary

Among 2D edge solitons, TPES are special in that their propagation through arbitrary boundaries can be described by 1D NLS. By contrast, non-topologically protected edge solitons around the corners are found to exhibit a combination of transmission, reflection and scattering into the bulk. Thus, the existence of TPES could serve as an important benchmark in incorporating nonlinearity into the design of perturbative topological metamaterials [56]. Compared to photonic TIs, mechanical TIs contain much simpler components, which may allow TPES to be observed in tabletop experiments. Moreover, the time reversal symmetry of mechanical systems implies bidirectional wave propagation and thus potentially richer dynamics than their photonic counterparts.

In summary, we have realized edge solitons theoretically and numerically in a 2D nonlinear mechanical topological insulator exhibiting the QSHE. The derivation can be readily generalized to other mechanical TIs with discrete elements [17, 57], possibly with dissipation [58] and forcing [20] included. Further extensions may include TIs in nonlinear continuous media, such as recent proposals based on magnetic solitons [59] and water waves [60].

The tunable and lossless nature of TPES may have significant impacts on existing applications of TIs such as optical and acoustic delay lines [61, 62] and robust manipulation of light and sound [63, 64]. In photonic TIs, TPES have been applied to nonlinear filtering and switching [36] and optical isolation [65]; analogs in mechanical TIs may soon emerge. Future applications of TPES to logic devices may benefit from the possibility for collision-based computing provided by such nonlinear coherent structures [66].

## Acknowledgements

Y.M. acknowledges support from a Vice Chancellor's Research Fellowship at Northumbria University. The authors would like to thank the two anonymous referees for their insightful comments.

## References

[1] S. D. Huber, Topological mechanics, Nature Physics 12 (2016) 621.
[2] G. Ma, P. Sheng, Acoustic metamaterials: From local resonances to broad horizons, Science advances 2 (2016) e1501595.
[3] J. E. Moore, The birth of topological insulators, Nature 464 (2010) 194.
[4] M. Z. Hasan, C. L. Kane, Colloquium: topological insulators, Reviews of Modern Physics 82 (2010) 3045.
[5] X.-L. Qi, S.-C. Zhang, Topological insulators and superconductors, Reviews of Modern Physics 83 (2011) 1057.
[6] X.-L. Qi, Y.-S. Wu, S.-C. Zhang, General theorem relating the bulk topological number to edge states in two-dimensional insulators, Physical Review B 74 (2006) 045125.
[7] C.-K. Chiu, J. C. Teo, A. P. Schnyder, S. Ryu, Classification of topological quantum matter with symmetries, Reviews of Modern Physics 88 (2016) 035005.
[8] F. Haldane, S. Raghu, Possible realization of directional optical waveguides in photonic crystals with broken time-reversal symmetry, Physical review letters 100 (2008) 013904.
[9] L. Lu, J. D. Joannopoulos, M. Soljačić, Topological photonics, Nature Photonics 8 (2014) 821.

[10] T. Ozawa, H. M. Price, A. Amo, N. Goldman, M. Hafezi, L. Lu, M. Rechtsman, D. Schuster, J. Simon, O. Zilberberg, et al., Topological photonics, arXiv preprint arXiv:1802.04173 (2018).

[11] Z. Wang, Y. Chong, J. D. Joannopoulos, M. Soljačić, Observation of unidirectional backscattering-immune topological electromagnetic states, Nature 461 (2009) 772.

[12] A. B. Khanikaev, S. H. Mousavi, W.-K. Tse, M. Kargarian, A. H. MacDonald, G. Shvets, Photonic topological insulators, Nature materials 12 (2013) 233.

[13] M. C. Rechtsman, J. M. Zeuner, Y. Plotnik, Y. Lumer, D. Podolsky, F. Dreisow, S. Nolte, M. Segev, A. Szameit, Photonic floquet topological insulators, Nature 496 (2013) 196.

[14] C. Kane, T. Lubensky, Topological boundary modes in isostatic lattices, Nature Physics 10 (2014) 39.

[15] L. M. Nash, D. Kleckner, A. Read, V. Vitelli, A. M. Turner, W. T. Irvine, Topological mechanics of gyroscopic metamaterials, Proceedings of the National Academy of Sciences 112 (2015) 14495–14500.

[16] R. Süsstrunk, S. D. Huber, Observation of phononic helical edge states in a mechanical topological insulator, Science 349 (2015) 47–50.

[17] R. K. Pal, M. Schaeffer, M. Ruzzene, Helical edge states and topological phase transitions in phononic systems using bilayered lattices, Journal of Applied Physics 119 (2016) 084305.

[18] R. Süsstrunk, S. D. Huber, Classification of topological phonons in linear mechanical metamaterials, Proceedings of the National Academy of Sciences 113 (2016) E4767–E4775.

[19] B. G.-g. Chen, N. Upadhyaya, V. Vitelli, Nonlinear conduction via solitons in a topological mechanical insulator, Proceedings of the National Academy of Sciences 111 (2014) 13004–13009.

[20] R. K. Pal, J. Vila, M. Leamy, M. Ruzzene, Amplitude-dependent topological edge states in nonlinear phononic lattices, Physical Review E 97 (2018) 032209.

[21] M. J. Ablowitz, Nonlinear dispersive waves: asymptotic analysis and solitons, volume 47, Cambridge University Press, 2011.

[22] Y. V. Kartashov, B. A. Malomed, L. Torner, Solitons in nonlinear lattices, Reviews of Modern Physics 83 (2011) 247.

[23] E. Fermi, P. Pasta, S. Ulam, M. Tsingou, Studies of the nonlinear problems, Technical Report, Los Alamos Scientific Lab., N. Mex., 1955.

[24] S. Katz, S. Givli, Solitary waves in a bistable lattice, Extreme Mechanics Letters 22 (2018) 106 – 111.

[25] I. A. Butt, J. A. Wattis, Discrete breathers in a two-dimensional hexagonal fermi–pasta–ulam lattice, Journal of Physics A: Mathematical and Theoretical 40 (2007) 1239.

[26] F. Chen, M. Herrmann, Kdv-like solitary waves in two-dimensional fpu-lattices, arXiv preprint arXiv:1703.10358 (2017).

[27] A. Pikovsky, M. Rosenblum, J. Kurths, J. Kurths, Synchronization: a universal concept in nonlinear sciences, volume 12, Cambridge university press, 2003.

[28] J. Cuevas, L. Q. English, P. G. Kevrekidis, M. Anderson, Discrete breathers in a forced-damped array of coupled pendula: modeling, computation, and experiment, Physical review letters 102 (2009) 224101.

[29] Y. Xu, T. Alexander, H. Sidhu, P. G. Kevrekidis, Instability dynamics and breather formation in a horizontally shaken pendulum chain, Physical Review E 90 (2014) 042921.

[30] F. Palmero, J. Han, L. Q. English, T. Alexander, P. Kevrekidis, Multifrequency and edge breathers in the discrete sine-gordon system via subharmonic driving: Theory, computation and experiment, Physics Letters A 380 (2016) 402–407.

[31] C. Chong, M. A. Porter, P. Kevrekidis, C. Daraio, Nonlinear coherent structures in granular crystals, Journal of Physics: Condensed Matter 29 (2017) 413003.

[32] R. Chaunsali, E. Kim, A. Thakkar, P. G. Kevrekidis, J. Yang, Demonstrating an in situ topological band transition in cylindrical granular chains, Physical review letters 119 (2017) 024301.

[33] M. Ablowitz, B. Prinari, Nonlinear schrodinger systems: continuous and discrete, Scholarpedia 3 (2008) 5561.

[34] M. J. Ablowitz, C. W. Curtis, Y.-P. Ma, Linear and nonlinear traveling edge waves in optical honeycomb lattices, Physical Review A 90 (2014) 023813.

[35] M. J. Ablowitz, Y.-P. Ma, Strong transmission and reflection of edge modes in bounded photonic graphene, Optics letters 40 (2015) 4635–4638.

[36] D. Leykam, Y. D. Chong, Edge solitons in nonlinear-photonic topological insulators, Physical review letters 117 (2016) 143901.

[37] Y. V. Kartashov, D. V. Skryabin, Modulational instability and solitary waves in polariton topological insulators, Optica 3 (2016) 1228–1236.

[38] D. R. Gulevich, D. Yudin, D. V. Skryabin, I. V. Iorsh, I. A. Shelykh, Exploring nonlinear topological states of matter with exciton-polaritons: Edge solitons in kagome lattice, Scientific Reports 7 (2017) 1780.

[39] C. Li, F. Ye, X. Chen, Y. V. Kartashov, A. Ferrando, L. Torner, D. V. Skryabin, Lieb polariton topological insulators, Physical Review B 97 (2018) 081103.

[40] T. Shi, H. Kimble, J. I. Cirac, Topological phenomena in classical optical networks, Proceedings of the National Academy of Sciences (2017) 201708944.

[41] C. L. Kane, E. J. Mele, Quantum spin hall effect in graphene, Physical review letters 95 (2005) 226801.

[42] B. A. Bernevig, S.-C. Zhang, Quantum spin hall effect, Physical review letters 96 (2006) 106802.

[43] D. R. Hofstadter, Energy levels and wave functions of bloch electrons in rational and irrational magnetic fields, Physical review B 14 (1976) 2239.

[44] J. Ginibre, G. Velo, The global cauchy problem for the non linear klein-gordon equation, Mathematische Zeitschrift 189 (1985) 487–505.

[45] A. Shabat, V. Zakharov, Exact theory of two-dimensional self-focusing and one-dimensional self-modulation of waves in nonlinear media, Soviet physics JETP 34 (1972) 62.

[46] See Supplementary Material. This includes the equations of motion adapted from [16], further analysis, and simulation videos.

[47] S. R. Sklan, B. Li, A unified approach to nonlinear transformation materials, Scientific reports 8 (2018) 4436.

[48] C. Kharif, E. Pelinovsky, Physical mechanisms of the rogue wave phenomenon, European Journal of Mechanics-B/Fluids 22 (2003) 603–634.

[49] A. Chabchoub, N. Hoffmann, N. Akhmediev, Rogue wave observation in a water wave tank, Physical Review Letters 106 (2011) 204502.

[50] K. B. Dysthe, K. Trulsen, Note on breather type solutions of the nls as models for freak-waves, Physica Scripta 1999 (1999) 48.

[51] Y. V. Bludov, V. Konotop, N. Akhmediev, Matter rogue waves, Physical Review A 80 (2009) 033610.

[52] D. Peregrine, Water waves, nonlinear schrödinger equations and their solutions, The ANZIAM Journal 25 (1983) 16–43.

[53] Y.-C. Ma, The perturbed plane-wave solutions of the cubic schrödinger equation, Studies in Applied Mathematics 60 (1979) 43–58.

[54] N. Akhmediev, V. Eleonskii, N. Kulagin, Exact first-order solutions of the nonlinear schrödinger equation, Theoretical and mathematical physics 72 (1987) 809–818.

[55] E. Charalampidis, J. Lee, P. Kevrekidis, C. Chong, Phononic rogue waves, arXiv preprint arXiv:1801.06086 (2018).

[56] K. H. Matlack, M. Serra-Garcia, A. Palermo, S. D. Huber, C. Daraio, Designing perturbative metamaterials from discrete models, Nature materials 17 (2018) 323.
[57] G. Salerno, A. Berardo, T. Ozawa, H. M. Price, L. Taxis, N. M. Pugno, I. Carusotto, Spin–orbit coupling in a hexagonal ring of pendula, New Journal of Physics 19 (2017) 055001.
[58] Y. Xiong, T. Wang, P. Tong, The effects of dissipation on topological mechanical systems, Scientific reports 6 (2016) 32572.
[59] S. K. Kim, Y. Tserkovnyak, Chiral edge mode in the coupled dynamics of magnetic solitons in a honeycomb lattice, Physical review letters 119 (2017) 077204.
[60] S. Wu, Y. Wu, J. Mei, Topological helical edge states in water waves over a topographical bottom, New Journal of Physics 20 (2018) 023051.
[61] M. Hafezi, E. A. Demler, M. D. Lukin, J. M. Taylor, Robust optical delay lines with topological protection, Nature Physics 7 (2011) 907.
[62] Z. Zhang, Y. Tian, Y. Cheng, Q. Wei, X. Liu, J. Christensen, Topological acoustic delay line, Physical Review Applied 9 (2018) 034032.
[63] X. Cheng, C. Jouvaud, X. Ni, S. H. Mousavi, A. Z. Genack, A. B. Khanikaev, Robust reconfigurable electromagnetic pathways within a photonic topological insulator, Nature materials 15 (2016) 542.
[64] S. Yves, R. Fleury, F. Lemoult, M. Fink, G. Lerosey, Topological acoustic polaritons: robust sound manipulation at the subwavelength scale, New Journal of Physics 19 (2017) 075003.
[65] X. Zhou, Y. Wang, D. Leykam, Y. D. Chong, Optical isolation with nonlinear topological photonics, New Journal of Physics 19 (2017) 095002.
[66] A. Adamatzky, J. Durand-Lose, Collision-based computing, in: Handbook of Natural Computing, Springer, 2012, pp. 1949–1978.

# Supplementary Material:
## Edge Solitons in a Nonlinear Mechanical Topological Insulator

David D. J. M. Snee and Yi-Ping Ma

The Supplementary Material here is organized into five sections and accompanying films for the bright and dark soliton simulations. In the first section we enclose the method used to construct edge solitons with non-zero background. The second section then looks closely at the bright and dark solitons and shows that the theoretically predicted NLS amplitude derived from the asymptotic analysis is the most efficient amplitude for the evolution of solitons in the system. Next we explore the interaction of two bright NLS solitons initialized on the same lattice and qualitatively show the phase shift that occurs in such a collision. We then consider the propagation of bright and dark solitons on domains with finer length scales to further show the topological protection of such nonlinear waves. Finally we verify the nonlinear theory further by exploring gray soliton and Akhmediev breather solutions to the classical 1D NLS, and realize them in this mechanical topological insulator.

### CONSTRUCTION OF EDGE SOLITONS

To facilitate initialization of the non-zero background one must compute the full 2D profile, which is a linear combination of 2D eigenfunctions $\boldsymbol{X}^i_{r,S}$, based on the criterion that the left edge contains precisely the initial condition Eq. (12). Formally, given the 1D soliton profile, say $C_D(S)$, and a set of wavenumbers $k_i$, we need to use an inverse discrete Fourier transform (IDFT) to find the coefficients $X_i$ such that

$$C_D(S)e^{ik_0S} = \sum_i X_i e^{ik_iS}. \tag{S1}$$

For each 2D eigenvalue there exists a set of 2 orthogonal 2D eigenfunctions that we may restrict to the left edge ($r = 0$) and write in the form $\boldsymbol{u}_1 = \cos(k_iS + \theta)$ and $\boldsymbol{u}_2 = \sin(k_iS + \theta)$, each with the dual harmonics $\pm k_i$. We can isolate the $\pm k_i$ harmonic by forming the linear combination $\boldsymbol{u}_1 \pm i\boldsymbol{u}_2$. The 2D eigenfunctions are then normalized to make the left edge of the form $e^{ik_iS}$ by finding a scaling factor $g_i\boldsymbol{X}^i_{r,S} = \boldsymbol{X}^E_r$ such that the values of all 6 variables in the central cell ($S = S_0$) agree with the 1D eigenfunction in the least squares sense. The 2D eigenfunctions are now recast into a form most compatible with the initial condition Eq. (12).

We then compute the IDFT to find the coefficients $X_j$: multiplying Eq. (S1) by $e^{-ik_jS}$ and summing over $S$ leads us to

$$X_j = \sum_S e^{-ik_jS}\frac{C_D(S)e^{ik_0S}}{L_S}, \tag{S2}$$

where $L_S$ is the number of cells.

The wavenumber $k_j$ can be determined accurately by utilizing the following relationship between neighboring cells of a particular component, say $x^{(0)}_{r=0,S}$:

$$x^{(0)}_{r=0,S=n+1} = e^{ik_j}x^{(0)}_{r=0,S=n}, \tag{S3}$$

where $n$ is a cell location sufficiently far enough away from the corners of the lattice. Rearranging Eq. (S3) allows us to explicitly write the wavenumbers as $k_j = \mathcal{R}e(-i\log_e(x^{(0)}_{r=0,S=n+1}/x^{(0)}_{r=0,S=n}))$.

Finally, we need to choose $L_S$ such that the wavenumbers on the left edge extracted from the 2D eigenfunctions agree with the wavenumbers on the 1D periodic domain. The wavenumbers for successive 2D eigenfunctions are approximately equally spaced whilst, on a 1D periodic domain of length $L_S$, the spacing between the wavenumbers of successive eigenfunctions is $2\pi/L_S$. The equality of the two wavenumber spacings determines $L_S$, which generally may not be an integer. This is an inherent imperfection of our method that we aim to fix in the future.

The 2D profile can then be constructed as the linear combination of the normalized 2D eigenfunctions:

$$X_{r,S}(t = 0) = \sum_j X_j\boldsymbol{X}^j_{r,S} + c.c. \tag{S4}$$

### THE NLS AMPLITUDE

We will now consider what happens when we force an amplitude other than the one predicted by the asymptotic analysis onto the bright soliton envelope (13) and the dark soliton envelope (14) whilst keeping the other parameters unchanged.

Firstly, let us take the bright edge soliton in Fig. 3(a), with wavenumber $k_0 = 2.827$, frequency $\alpha_0 = 12.506$, and theoretically predicted NLS amplitude $\Lambda = 1.376$, as a case study for the varied amplitudes. The nonlinear wave travels clockwise around the domain, completing a full cycle with a period of about 300. The longtime profile of this edge soliton shows little decay as seen in Fig. S1(a): at $t \approx 2000$ ($t \approx 4000$), the soliton has completed about 6 (12) cycles of the domain and the soliton amplitude has only decayed to approximately 96% (93%) of its initial theoretically predicted value.

Taking a smaller amplitude than the theoretically predicted results in a compelling amount of decay of the

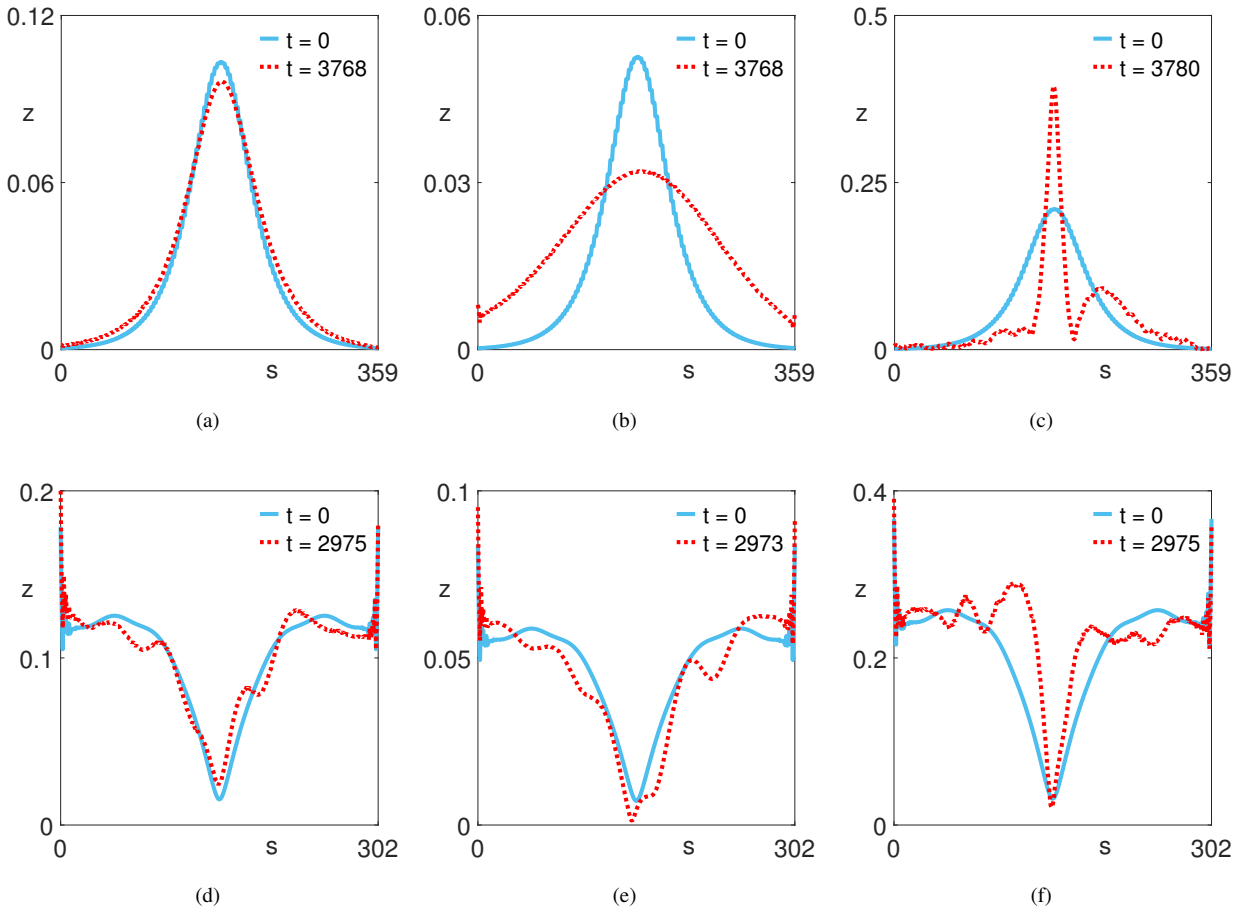


Figure S1: (Color online) Propagation of solitons with differing amplitudes. (a,b,c) Bright solitons on a rectangular lattice of size $N_r \times N_S = 30 \times 120$ with carrier wavenumber and frequency $(k_0, \alpha_0) = (2.827, 12.506)$, and soliton amplitudes (a) $\Lambda = 1.376$; (b) $\Lambda = 0.7$; (c) $\Lambda = 2.8$. (d,e,f) Dark solitons on a rectangular lattice of size $N_r \times N_S = 30 \times 101$ with carrier wavenumber and frequency $(k_0, \alpha_0) = (2.146, 13.616)$, and soliton amplitudes (d) $\Lambda = 1.705i$; (e) $\Lambda = 0.8i$; (f) $\Lambda = 3.5i$. Profiles are taken initially (blue-solid) and after a long time interval (red-dashed). Solitons (a) and (d) are precisely the solitons with theoretically predicted NLS amplitudes seen in Fig. 3.

bright soliton profile. This is seen in Fig. S1(b) where we have considered an amplitude that is approximately half of the predicted, i.e. $\Lambda = 0.7$. Here, the peak of the soliton has decayed to 61% of its original value long after the initial time ($\approx 4000$ time units), which is a significant decrease in comparison to the 93% seen before (Fig. 1(a)). Moreover, the Gaussian profile has dispersed out to the point where the tail ends of the bright soliton are cut off by the corners of the 2D rectangular domain. In contrast to this, Fig. S1(c) shows the effect of initializing a larger amplitude, where we have considered approximately double the theoretically predicted, i.e. $\Lambda = 2.8$. We see that this has a severe consequence on the structure of the bright soliton and the crest of the initial Gaussian curve has almost doubled in size; the remainder of the soliton has a somewhat random structure to it. This phenomenon is down to an overfocusing effect where the energy to the immediate left and right of the initial peak has been redistributed to the peak itself.

The dark soliton can be explored in a similar manner by initializing an amplitude of half and double the theoretically predicted, seen in Figures S1(e) and S1(f) respectively. These two profiles are comparable to the dark soliton profile in Fig. S1(d) with the predicted amplitude $\Lambda = 1.705i$, wavenumber $k_0 = 2.146$, and corresponding frequency $\alpha_0 = 13.616$. As shown in Fig. S1(d), at $t \approx 4000$ the general structure of the dark soliton has not altered much at all and the fluctuations in the carrier wave are caused by the imperfectly constructed initial condition. Taking an amplitude which is less than

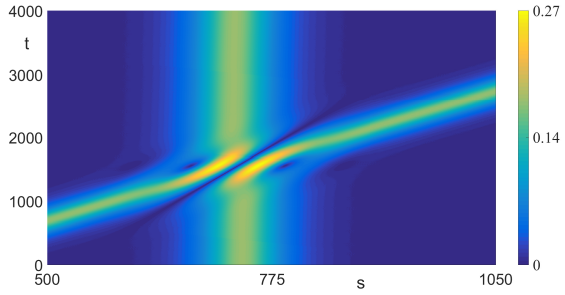


Figure S2: (Color online) Phase shift of a bright soliton directly after the interaction with another bright soliton on a rectangular lattice of $9 \times 350$ cells, with periodic boundary conditions on the top and bottom edges. The co-moving soliton has carrier wavenumber and frequency $(k_0, \alpha_0) = (0.524, 11.138)$, which leads to soliton amplitude $\Lambda = 2.345$ in Eq. (13), whilst the interacting soliton has $(k_0, \alpha_0) = (0.7850, 11.219)$ and $\Lambda = 2.306$.

that of the theoretically predicted, we see that the trough of the dark soliton widens. Contrary to this, taking an initial amplitude which is greater than that of the theoretically predicted causes a narrowing and distortion in the envelope itself; sporadic fluctuations are also produced in the carrier wave. Therefore, we see once again that the NLS amplitude is the best amplitude for the evolution of the dark soliton.

Overall, it is clear that the amplitude theoretically predicted by the NLS equation (11) which governs the envelope of these nonlinear traveling waves is truly the best amplitude for the formation of solitons in this MTI. If one considers an initial amplitude other than this then the nonlinear and dispersive terms are no longer balanced causing effects such as overfocusing and severe profile distortion as the soliton evolves in time.

## INTERACTION OF TWO BRIGHT SOLITONS

Let us now initialize two bright solitons on the same edge of the MTI and allow them to collide. For this we move to an $s$-periodic domain and transfer to the co-moving frame of one of the waves to best visualize the structure of the collision. Since the waves are nonlinear we expect that the interaction should not be a simple linear superposition of the two waves.

Figure S2 shows the interaction of the two bright solitons on a periodic domain of $9 \times 350$ cells. Here we allow both waves to travel up the periodic edge with one wave having a greater group velocity, thus catching the other wave some time after initializing. The slower soliton has wavenumber $k_0 = 0.524$ and corresponding frequency $\alpha_0 = 11.138$, whilst the faster soliton has wavenumber $k_0 = 0.785$ and frequency $\alpha_0 = 11.219$.

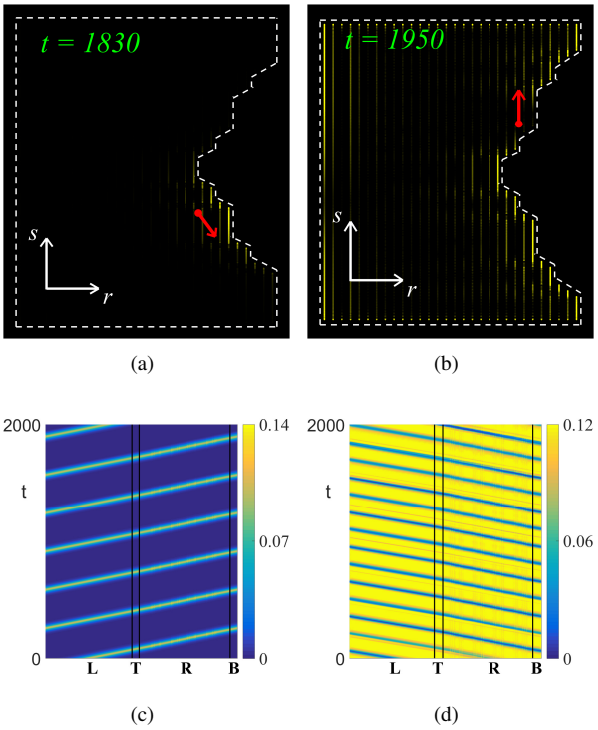


Figure S3: (Color online) Propagation of bright and dark solitons on a finer domain. The 2D domain consists of a rectangular lattice with a Cantor-like design cut out of the right edge. (a,c) A bright soliton with same parameters as in Fig. 3(a,c,e). (b,d) A dark soliton with the same parameters featured in Fig. 3(b,d,f). As in Fig. 3, panels (a,b) show snapshots of the respective soliton as it propagates through the irregular edge. Red arrows indicate the position and direction of the soliton envelope. panels (c,d) show space-time plots of the edge solitons traversing the irregular domain multiple times.

Here we transfer into the co-moving frame of the slower wave. The figure shows that immediately after the collision has occurred, the faster wave has passed through the slower with both structures intact and with the same amplitude and group velocity as before. However, the slower wave has been visibly phase-shifted as a direct consequence of the nonlinear collision.

## DOMAINS WITH FINER LENGTH SCALES

The concept of TPES has already been shown for rectangular domains and domains with sharp corners cut into the middle of an edge, however we are not limited to domains of these type. We show here a further example of the topological protection of solitons on an edge with a rough structure carved into the lattice that adopts a Cantor-like design.

Figure S3 shows the propagation of bright and dark edge solitons around the domain with finer length

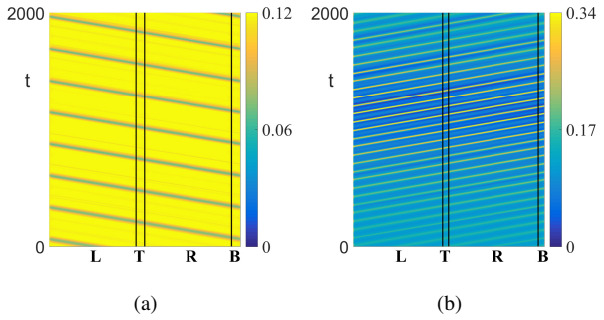


(a) (b)

Figure S4: (Color online) Panel (a) shows the propagation of a gray soliton on a rectangular lattice of 30×101 cells with carrier wavenumber and frequency $(k_0, \alpha_0) = (2.146, 13.616)$, parameter $\psi = \pi/3$, and soliton amplitude $\Lambda = 0.1705i$ given by Eq. (S5). Panel (b) shows the appearance of an Akhmediev breather described by Eq. (S6) on a rectangular lattice of $20 \times 100$ cells, with carrier wavenumber and frequency $(k_0, \alpha_0) = (2.334, 12.113)$, that peaks at $t \approx 1200$ with modulation parameter $\phi = 0.6$.

scales. Notably we see that both types of soliton traverse the irregular domain with little change in the structure of the initial pulse. This is expected from TPES as, regardless of the edge shape, we expect such unique nonlinear waves to pass through irregular edges without major backscattering of the energy. We do however note the appearance in Fig. S3(d) of an extra gray soliton stemming from the initial condition on the right edge of the lattice. This gray soliton appears due to an imperfection in the 2D reconstruction method but we note that this extra soliton is also topologically protected, showing exactly the robust nature of TPES when generated.

## GRAY SOLITON AND AKHMEDIEV BREATHER

We have already seen particular examples of traveling and rogue wave solutions realized in this mechanical topological insulator. However, any solution to the classical 1D NLS equation should theoretically produce an analogue structure in our system. Here we realize two more solutions of 1D NLS including the gray soliton and the Akhmediev breather.

Let us first consider another traveling wave solution which is the gray soliton. The gray soliton appears as a localized dip in energy, but unlike the dark soliton, it is not limited to an envelope minimum of strictly zero amplitude. The gray soliton envelope takes a form similar to that of the dark soliton and is given explicitly as

$$C_G(S;\psi) = \Lambda\left[\cos\psi + i\sin\psi\tanh\tilde{\psi}\right], \qquad \text{(S5)}$$

with $\tilde{\psi} = \epsilon(S - S_0)\sin\psi$ and $\psi$ an arbitrary real parameter. We see that the dip in energy is then described by the $\sin\psi$ term and choosing $\psi = \pi/2$ recovers the dark envelope (14). Figure S4(a) shows the space-time evolution of a gray soliton initialized with wavenumber $k_0 = 2.146$, frequency $\alpha_0 = 13.616$, and $\psi = \pi/3$ on a rectangular domain. As expected, the evolution of the gray soliton is in fact similar to the dark soliton for the same wavenumber-frequency pairing, with a primarily undistorted profile throughout the evolution and little decay in the background field after a long time interval.

Finally, let us explore another rogue wave solution known as the Akhmediev breather [54]. In contrast to the K-M soliton which is time-periodic, the Akhmediev breather is a spatially periodic solution that is localized in time. The scalar envelope function is given by the Akhmediev expression in [50], i.e.

$$C_A(S;\phi) = \Lambda\left[\frac{\cosh(\Omega\tilde{t}_0 + 2i\phi) - \cos\phi\cos\bar{S}}{\cosh(\Omega\tilde{t}_0) - \cos\phi\cos\bar{S}}\right]e^{i\tilde{\theta}}, \qquad \text{(S6)}$$

where $\tilde{\theta} = \alpha_0 t_0 - \tilde{t}_0$, $\tilde{t}_0 = \epsilon^2\alpha_0'' t_0$, $\bar{S} = P\epsilon(S - S_0)$, $P = 2\sin\phi$, and $\Omega = \sin 2\phi$. As with the Peregrine soliton, we initialize the time-localized structure well before its maximum amplitude, which is designed to appear at time $t_0 = 1200$. Note that one can recover the K-M solution (16) from the Akhmediev expression by using the parameter transformation $\phi \to i\phi$. Figure S4(b) shows the appearance of an Akhmediev breather. It is clear to see the spatially periodic nature of the breather as all peaks form their maximum amplitude at $t \approx t_0$ and then decay away beyond this time which is consistent with the analytic solution (S6). The Peregrine soliton (15) is in fact the limiting case ($\phi \to 0$) of both the K-M soliton and the Akhmediev breather.